Establishment of AIRS Climate-Level Radiometric Stability using Radiance Anomaly Retrievals of Minor Gases and SST

L. Larrabee Strow and Sergio DeSouza-Machado

Dept of Physics and JCET, University of Maryland Baltimore County, Baltimore, Maryland

Correspondence: L. Larrabee Strow (strow@umbc.edu)

Abstract. Temperature, H_2O, and O_3 profiles, as well as CO_2, N_2O, CH_4, CFC12, and SST scalar anomalies are computed using a clear subset of AIRS observations over ocean for the first 16-years of NASA's EOS-AQUA AIRS operation. The AIRS Level 1c radiances are averaged over 16 days and 40 equal-area zonal bins and then converted to brightness temperature anomalies. Geophysical anomalies are retrieved from the brightness temperature anomalies using a relatively standard

5 optimal estimation approach. The CO_2, N_2O, CH_4, and CFC12 anomalies are derived by applying a vertically uniform multiplicative shift to each gas in order to obtain an estimate for the gas mixing ratio. The minor gas anomalies are compared to the NOAA ESRL in-situ values and used to estimate the radiometric stability of the AIRS radiances. Similarly the retrieved SST anomalies are compared to the SST values used in the ERA-Interim reanalysis and to NOAA's OISST SST product. These inter-comparisons strongly suggest that many AIRS channels are stable to better than 0.02 to 0.03 K/Decade, well be-

10 low climate trend levels, indicating that the AIRS blackbody is not drifting. However, detailed examination of the anomaly retrieval residuals (observed minus computed) show various small unphysical shifts that correspond to AIRS hardware events (shutdowns, etc.). Some examples are given highlighting how the AIRS radiances stability could be improved, especially for channels sensitive to N_2O and CH_4. The AIRS short wave channels exhibit larger drifts that make them unsuitable for climate trending, and they are avoided in this work. The AIRS Level 2 surface temperature retrievals only use short wave channels. We

15 summarize how these short wave drifts impacts recently published comparisons of AIRS surface temperature trends to other surface climatologies.

1 Introduction

The Atmospheric Infrared Sounder (AIRS) on NASA's AQUA satellite platform (Aumann et al., 2003) measures 2378 high-spectral resolution infrared radiances between 650 and 2665 cm^{-1} with a resolving power ($\lambda/\Delta\lambda$) of ~1200. Launched in 2002

20 into a sun-synchronous polar orbit with a 13:30 ascending node equator crossing time, AIRS now has been operating almost continuously for 17+ years.

The long record of AIRS allows measurements of short-term climate trends that are especially useful given it's global coverage. Nominal decadal climate temperature trends are in the 0.1-0.2K/decade range. For example a recent Intergovernmental Panel on Climate Change (IPCC) report (Masson-Delmotte et al., 2018) suggests 20th century trends (2000-2017) of about

25 0.17K/decade. If AIRS is to contribute to climate-level trend measurements, uncertainty estimates for the time stability of the

AIRS radiances are a pre-requisite before using AIRS Level 2/3 products for climate level trending. Estimating the level of any instrument-related trends, for a wide range of AIRS channels, is the subject of this work.

A recent study (Aumann et al., 2019) addressed the stability of a single AIRS channel by comparisons to sea surface temperatures. Some limitations of this study are addressed below, but the major limitation of this work is that AIRS retrievals use 400+ AIRS channels, and there is no guarantee that the AIRS stability in one channel applies to all channels, as acknowledged in (Aumann et al., 2019).

AIRS is sensitive to a host of atmospheric and surface variables, including atmospheric temperature (via CO_2 emissions), humidity, surface temperature, O_3, CH_4, N_2O, carbon monoxide, clouds, coarse mode aerosols and other minor gases. 1D-var retrievals such as the AIRS Level 2 products (Susskind et al., 2014) attempt to retrieve all relevant atmospheric and surface variables in order to produce the most accurate temperature and H_2O profiles. The atmospheric CO_2 concentration is especially important for AIRS retrievals since most of the radiance measured in the temperature sounding channels is due to CO_2 emission. However, it is difficult to separate the CO_2 concentration from variations in the temperature profile due to co-linearity of their Jacobians. Consequently, the AIRS Level 2 retrievals instead vary CO_2 in the forward model to account for CO_2 growth during the mission (Blaisdell, 2019).

The largest radiance trends seen by AIRS are due to the growth rate of CO_2 in the atmosphere. Assuming a nominal growth rate of 2 ppm/year, and max sensitivity of AIRS channels of CO_2 of 0.03K/ppm, the brightness temperature (BT) shift in AIRS over 16-years is ~1K, or 0.06K/year. Concentrations of atmospheric carbon dioxide have been measured worldwide for many years with extremely high accuracy (Masarie and Tans, 1995; Tans and Keeling) by NOAA Earth System Research Laboratory (ESRL). Averaged yearly, CO_2 concentrations are highly uniform globally, with little latitudinal variation in growth rates. Similarly NOAA ESRL also provides a wide network of measurements of N_2O and CH_4, which are also relatively uniformly mixed over yearly time-periods. Here we use the high accuracy of the trends in these in-situ measurements of minor gases to determine the stability of a large number of AIRS channels.

Sea surface temperature (SST) trends are also extremely well measured and generally referenced to the in-situ ARGO (Argo, 2019) buoy network but interpolated to a full grid using instruments such as the AVHRR. Two SST products referenced to the buoy network are compared to AIRS trends here: (1) NOAA's Optimum Interpolation SST (version 2) (OISST) (Banzon et al., 2016), and (2) the Operational Sea Surface Temperature and Ice Analysis (OSTIA) (Stark et al., 2007), which has been used in the ERA-I Interim Reanalysis (ERA-I) since 2009 (Dee et al., 2011). Prior to Feb. 2009 ERA-I used the NCEP Real-Time Global SST (RTG) product, a precursor to OISST.

AIRS stability is referenced to trends in these minor gases and SST by performing 1D-var retrievals of clear scene radiance anomalies averaged into 40 equal-area latitude bins and 16-day time periods. Comparisons of the retrieved gas concentrations and SST trends, combined with examination of the retrieval residuals, provides a number of powerful tests of AIRS radiometric stability as well as detailed information on AIRS performance changes due to several minor instrument shutdowns that took place occasionally over the mission.

After a summarizing the characteristics of the AIRS instrument, and the data used in this work, the retrieval methodology is reviewed with a short discussion of the retrieved temperature profile time series. We follow with stability estimates derived

from the anomaly spectra retrievals of CO_2, N_2O, CH_4, and SST. Although AIRS is most sensitive to the two best in-situ data sets, CO_2 and SST, we also compare to retrievals of N_2O and CH_4 since they are also relatively well measured and help test the AIRS performance in spectral regions not covered by CO_2 and SST. Finally we examine the time series of the anomaly retrieval residuals (BT observed - fit) time series since, together with the anomaly geophysical retrievals, they provide detailed

65 information on AIRS radiances over time, especially the instrument response to various short shutdowns that occurred during the mission.

2 AIRS Instrument and Data

Several details of the AIRS instrument design are relevant to the processing performed here and are needed to understand some of the results. AIRS has 2378 spectral channels divided up into 17 different detector arrays. Appendix A gives the nominal

70 wavenumber boundaries of these arrays. Arrays M-11 and M-12 are linear arrays of single photoconductive HgCdTe detectors. The other AIRS arrays are photovoltaic detectors, and each reported detector output is actually some linear combination of two detectors offset from each other in the vertical (not dispersive) direction. The photovoltaic detectors for each AIRS channels are labeled "A" and "B". The relative contributions of A and B detectors can be changed by command to the spacecraft. The majority of these detectors are wired for equal contributions by the A and B detectors, which we denote as A+B detectors.

75 However, some detectors have always been inoperable, or their performance characteristics changed in orbit, so there are a number of A-only and B-only detectors.

The radiometric and spectral characteristics of the A versus B detectors can be slightly different. During the mission, good A+B detectors can suddenly exhibit greatly increased noise when one or the other of the two detectors fails or degrades. In many circumstances the AIRS Project has changed A+B detectors to be either A-only or B-only in order to recover that

80 particular channel, albeit at slightly lower noise levels than if both detectors were working properly. Fortunately, many of the A-only and B-only detectors are in the window regions where AIRS has tremendous redundancy. Unfortunately, the M-10 array which covers the tropospheric CO_2 sounding channels also has a good number of A-only, B-only detectors.

Here we avoid any photovoltaic channel that is not A+B, and any channel with a state change during the mission. Although A-only and B-only channels may perform well, many of these single detector channels exhibit drifts over the mission for colder

85 scenes. This is especially apparent in time series of cold scene observations (deep convective clouds) by comparison to similar time series derived from IASI on METOP-1. In addition, we avoid any channels with detector noise above 0.5K NEDT (for a 250K scene). As discussed below in more detail, we also avoid all short wave AIRS channels, meaning channels past 2000 cm^{-1} for our final trend measurements, since we find that the short wave is drifting slightly.

3 Radiance (BT) Anomalies

3.1 Clear Selection

AIRS L1c clear scenes are primarily detected using a uniformity filter. The BT of each AIRS ocean scene is subtracted from the BT of each of its 8 neighbors for two window channels at 819.3 and 961.1 cm^{-1}. A scene is deemed clear only if the absolute value of all of these differences, averaged over the two channels, is less than 0.4K. The selected scenes are matched to ERA-I model fields and a simulated clear BT for the 961.1 cm^{-1} channel is computed using a stand-alone version of the AIRS radiative transfer algorithm (Strow et al., 2003) called SARTA, implemented using HITRAN 2008 line parameters. If the difference between the observed and computed clear scene BT values is more than 4K the scene is discarded from the clear list. This test mostly removes colder scenes made up of very uniform marine boundary layer stratus clouds. The clear yield and mean zonal radiances are quite insensitive to the exact value of this threshold. The uniformity test is not performed on the first and last of the 135 along-track scans in each AIRS granule since they do not have 8 neighbors and we wanted to avoid cross-granule processing. The total number of clear scenes is limited to ~20,000 daily clear scenes by randomly sub-setting the detected clear scenes. In this work we only use descending node observations in order to avoid solar and nonLTE contributions to the AIRS radiances in the short wave.

All observing parameters, on a footprint basis, are saved, such as satellite viewing zenith angle and noise (converted to BT units).

The ERA-I model parameters (temperature, H$_2$O, and O$_3$ profiles, and surface temperature with a spatial resolution of approximately 80 km on 60 levels in the vertical from the surface up to 0.1 hPa.) are matched to each clear scene are also saved along with their associated simulated L1c radiances. The ERA-I profiles are used to compute the anomaly Jacobians, as discussed below. All of our processing can be tested using the simulated radiances rather than the observed radiances as input.

3.2 Clear Scene Characteristics

Figure 1 illustrates the density and location of the clear ocean dataset, averaged over 2012.

Retrievals are only performed on zonally averaged data, which translates into ~44/25 observations/day at -50°/+50° latitude respectively, with a maximum of 200 observations per day at -0.5° latitude. The non-uniform nature of this sampling should be kept in mind when examining temperature, H$_2$O, or O$_3$ trends in that this data set is not necessarily representative of global/zonal climate trends. However, we do assume that the minor gas anomaly trends we are retrieving are uniformly mixed over year+ time scales. Our anomaly retrieval results show uniform mixing is generally quite accurate over even 16-day time scales.

The ERA-I model fields, suitably converted to temperature, humidity, and ozone profile anomalies are used to compute the BT profile Jacobians needed for the anomaly retrievals. In principle we could have performed 1D-var retrievals on each 16-day averaged BT spectrum in each latitude zone. However, ERA-I is so accurate, that is not necessary. Figure 2 illustrates the accuracy of ERA-I for this dataset, where we show the (observed - ERA-I) based simulated BT bias for 28.4°N. This is the
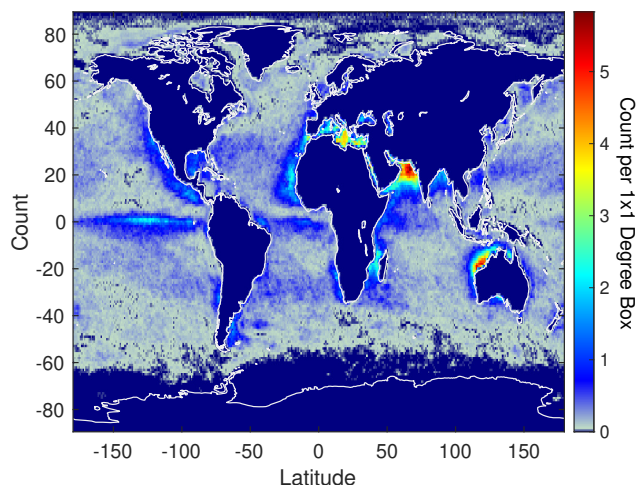
Figure 1. Density of AIRS clear ocean scene for calendar years 2012.

initial mean bias derived from a time-series fit to both the observed and ERA-I simulated time series, ie for time = 0 (Sept. 2002). The time series fit are discussed in Sect. 3.3.
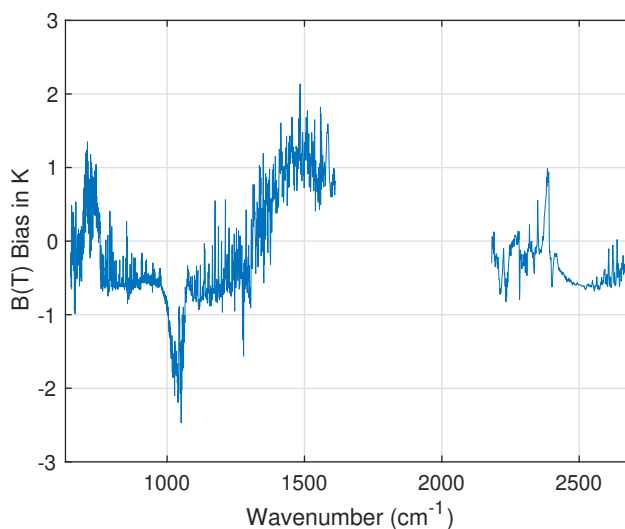
Figure 2. (AIRS - ERA-I simulated) BT bias for 28.4ºN in Sept. 2002. The CO_2 feature in the mid-wave near 700-760 cm^{-1} is due our use of a constant CO_2 concentration of 385 ppm for the ERA-I simulations, rather than a value ~370 ppm more appropriate for this date.

The CO_2 tropospheric sounding region in the 700-780 cm^{-1} region shows a sharp increase in the bias of about 0.6K (depend-ing on channel) that is due to the fact that the ERA-I based radiance simulations used a constant amount of CO_2 set at 385 ppm. This feature will go through zero bias and become negative by approximately the same BT amount at the end of our 16-year test period.

Figure 3 shows the linear trend for the clear dataset averaged over ±50° latitude.
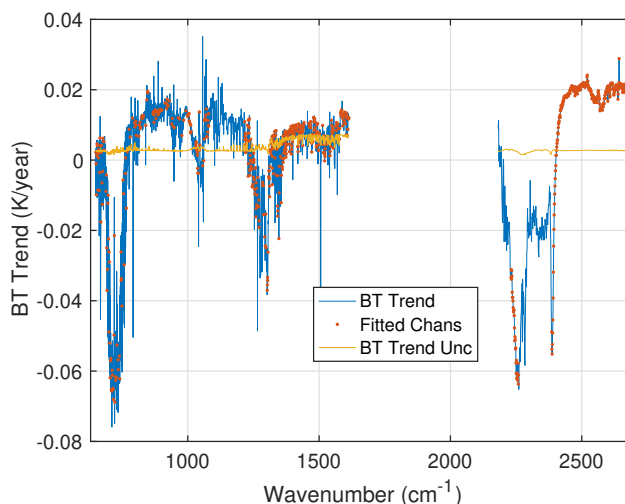
Figure 3. Mean radiance trends for ±50° in Δ BT/year units. The 2-σ uncertainty shown is lag-1 corrected for time series correlations. Channels used in the anomaly retrievals are denoted in red, and the BT trend uncertainty is in yellow.

These BT trends prominently exhibit the growth in CO_2 in the tropospheric channels from 700 to 750 cm^{-1}, which results in a negative change in the observed BT since increasing CO_2 shifts the emission to higher and therefore colder regions of the atmosphere. The growth in CO_2 in the stratospheric channels (a positive BT change) below 700 cm^{-1} is roughly cancelled by cooling in the stratosphere. All window channels exhibit warming, with larger values in the shortwave past 2450 cm^{-1}. The non-uniform spatial sampling of these clear scenes precludes any general statements about climate warming, although for these observations we clearly see warming, if the AIRS radiometry is stable. In addition, the effects of much stronger water vapor absorption in the long wave compared to the short wave windows makes definitive inter-comparisons of the BT trends complicated, which is addressed below by doing retrievals on these data.

3.3 Construction of Anomalies

The clear scene radiance subset is sorted into 40 equivalent area latitude bins that cover the full -90° to 90° latitude range and are averaged over every 16 days. This results in a data set for the first 16-years of AIRS that has the size 40 x 2645 x 365 denoting latitude bins, AIRS L1c channels, and the total number of 16-day averages. The following time-series function was fit to these averaged radiances for each latitude and AIRS L1c channel,

$$r(t) = r_o + a_1 t + \sum_i^4 c_i \sin(2\pi n t + \phi_i) \tag{1}$$

where t is AIRS mission times in years. The function models periodic variations in the radiances using an annual term and the first three harmonics. At 28°N, for example, the annual amplitude relative to the mean radiance, c_1/r_o, has a median value

10.5194/amt-2019-504
Atmospheric Measurement Techniques
2020-01-31
Author(s) 2020. CC BY 4.0 License.

(taken over channel) of 4.2%. The median amplitudes of the three harmonics terms, c_2, c_3, c_4 relative to r_o is 0.32%, 0.45%
and 0.23% respectively, all with 2-σ uncertainties of ~0.05%.

For the retrievals performed we created the radiance anomaly by inserting the linear trend into the residuals of the above
time series fits,

$$r_a(t) = r_{obs} - r(t) + a_1 t. \tag{2}$$

The linear term a_1 represents the linear-part of the minor gas signals we aim to measure. The a_1 terms are included in the
anomaly time-series fits since they are a useful way to quickly understand AIRS trends and because this allows us to measure
a more correct lag-1 auto-correlation of the time series noise, which is used to estimate corrections for the uncertainties in
the time-series parameters using the approach popularized in (Santer et al., 2000). The radiances anomalies were converted to
brightness temperature units

$$y(\nu) \equiv BT_a(\nu, t) = \frac{r_a(\nu, t)}{\frac{\partial r(\nu)}{\partial BT(\nu)}} \tag{3}$$

for our retrievals. The 40 x 2645 x 365 array of BT_a vectors are the retrieval inputs y as denoted in the retrieval formation
discussed in Sect. 4.

All uncertainties quoted in this paper derived from time series are for 95% uncertainty levels and are lag-1 corrected for
correlations in the time series residuals.
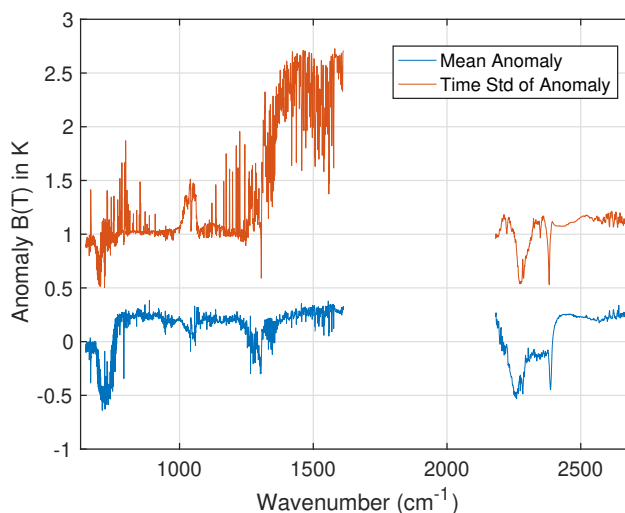
Figure 4. Mean and standard deviation of the AIRS BT anomalies for the zonal bin centered at 28.3ºN.

The anomaly BT time series mean BT spectra and their standard deviations are shown in Figure 4 for the 28.4ºN latitude
bin. The BT anomaly is set to zero at the mission start, therefore the mean BT in the CO_2 region is -0.5K given that it changes
by by ~-1K during the mission. The standard deviation indicates that the SST (and H_2O continuum) vary by ~1K during this

time period. Some of this is likely due to changes in sampling from day to day. The upper-tropospheric water vapor has the highest variability, which is expected due to both the variability of water vapor in time, and our non-uniform sampling.

An example radiance BT anomaly for the 710.141 cm⁻¹ channel is shown in Fig. 5, for the same latitude bin. This channel is
165 heavily influence by the CO_2 growth, so the AIRS observed trends are becoming more negative, although there is considerable noise, again due to weather and sampling. For comparison we also plot the ERA-I simulated BT anomaly, which does not contain the CO_2 growth, since it is set to a fixed value of 385 ppm in the simulations. The difference between these two BT anomalies will primarily be due to CO_2 growth, and is shown in black. Note that since the ERA-I tracks the atmospheric state quite accurately most of the time-series "noise" is removed. This helps lend credence to our use of the ERA-I model fields for
170 Jacobian evaluation.
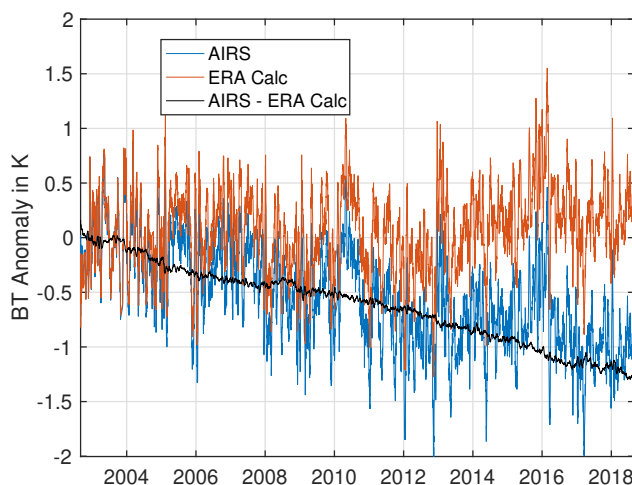
Figure 5. Sample AIRS observed and ERA-I simulated BT anomalies for the zonal bin centered at 28.3°N. The differences in the AIRS and ERA-I anomalies is plotted in black. Note, this difference anomaly is not used in the anomaly retrievals.

4 Retrieval Methodology

4.1 Approach

Geophysical retrievals are derived from BT anomalies, $y(\nu) \equiv BT_a(\nu, t)$, by minimizing the cost function J

$$J = (y - F(x))^T \mathbf{S}_\epsilon^{-1}(y - F(x)) + (x - x_a)^T \mathbf{R}(x)(x - x_a) \tag{4}$$

175 where $\mathbf{S}_\epsilon$ is a diagonal observation error covariance matrix containing the square of the BT noise, $\mathbf{K}$ are the anomaly Jacobians, and $\mathbf{R}$ is a regularization matrix. The retrieved atmospheric state x (the geophysical anomalies) are given by

$$x = x_a + (\mathbf{K}^T \mathbf{S}_\epsilon^{-1} \mathbf{K} + \mathbf{R})^{-1}(\mathbf{K}^T \mathbf{S}_\epsilon^{-1}(y - F(x_n))), \text{where } \mathbf{R} = \mathbf{S}_a^{-1} + \alpha \mathbf{L}^\mathbf{T} \mathbf{L}. \tag{5}$$

A-priori estimates for $x_a(t) \equiv 0$ for T(z), O_3(z), H_2O(z) and T_{SST} were set to zero. Two approaches were used for the minor gas a-priori estimates. The first approach set $x_a(t) = x_a(t-1)$ where $x_a(t=0) = 0$ for the minor gases, iteratively increasing the a-priori gas amount in time based on the previous 16-day retrieval.

Another approach used the known growth rates in the minor gases (from ESRL) by setting $x_a(t) = g*(t-t_o)$ for the a-priori minor gas amount, where g is the nominal yearly growth rate for each gas from the NOAA ESRL atmospheric gas trends. For both approaches we set the a-priori covariance to g times one year, the yearly variation in that gas. Nearly identical results are obtained if we used g times five years. The iterative approach for setting the minor gas a-priori produces noisier retrieval anomalies. However, if our retrievals are averaged over ± 50° latitude, both approaches produced identical differences compared to in-situ measurements, including error uncertainties. The figures shown here use the a-priori ramp from the ESRL data, although the figures for the iterative ramp are only distinguishable from what is shown for single zonal retrievals (such as the Mauna Loa and Cape Grim comparisons).

The retrieval approach is standard Optimal Estimation (OE) (Rodgers, 1976) enhanced to include both covariance and empirical Tikhonov regularization in **R** (Steck, 2002). Here we use Tikhonov L1-type derivative smoothing. Forward model uncertainty is not included in the measurement error covariance.

The temperature, H_2O, and O_3 profile retrievals use 20 atmospheric layers, selected from the AIRS standard 100-layer pressure grid (Strow et al., 2003) by accumulating five of the standard AIRS layers at a time. The lowest layer is about 1.5 km thick, with increasingly wider layers as you go higher in the atmosphere. This layering scheme allows more layers then degrees-of-freedom (DOFs) although it does limit retrievals in the upper-stratosphere. We wish to minimize our sensitivity to the upper-stratosphere since our comparisons to in-situ measurements are made in the troposphere. Consequently we removed all channels peaking above 10 hPa.

Most of the regularization in the retrieval comes from the Tikhonov terms, since we do not want to invoke climatology too strongly for a climate level measurement. Appendix B discusses the profile retrievals, and simulations of these retrievals, in more detail. In summary, after experimentation with Tikhonov regularization we added some a-priori covariance uncertainties in temperature and water vapor of 2.5K and 60% respectively. These a-priori covariance uncertainty terms improved simulated retrievals and profile trends generated from these retrievals by 3-10%.

The observation error covariances were derived by averaging the noise from each observations contributing to the averaged anomaly being retrieved. Originally a fixed value of 0.01K observation noise was used, but we found that this noise value depressed the CO_2 anomaly retrievals as they grew in size over time. This problem disappeared once we switched to the true measurement noise values, which are in the range of noise equivalent brightness temperature (NEDT) equal to 0.004K for long wave CO_2 channels, about 0.001K in window regions, and 0.001 to 0.002K in the water bands.

As stated earlier, the profile Jacobians used the ERA-I profiles, which were converted to anomaly profiles for each pressure layer. The minor gas Jacobians were computed using our pseudo line-by-line kCARTA radiative transfer algorithm (Strow et al., 1998; DeSouza-Machado et al., 2019). kCARTA allows for extremely accurate Jacobian calculations, including analytic trace gas and temperature Jacobians. Initial retrievals used a fixed value for the minor-gas Jacobians. However, given the large increase in the minor gases (10% for CO_2), we determined that the minor-gas Jacobians need to be updated as the gas amounts

increase. Therefore we used finite-difference Jacobians, computed using the minor gas amount retrieved from the previous
time-step during the anomaly retrievals (or from the gas amount estimated using NOAA ESRL in-situ gas amount data). The
215 minor gas profiles used in the Jacobian calculations are from (Anderson et al., 1986). The CO_2 profile is essentially constant
in ppm until you reach the highest atmospheric layer.

There exists a weak dependence of these retrievals on the ERA-I model fields since we use the ERA-I model fields for the
temperature, H_2O, and O_3 profiles in the profile Jacobians, **K**. While we could retrieve the atmospheric profiles from the full
radiance at each time step and latitude zone, ERA-I is so accurate we do not believe this is needed. Moreover, we *do* retrieve
220 the profile anomaly in each step, so we are not dependent on the actual ERA-I model values for the retrieval other than a weak
dependence via the Jacobians. In the results shown later the impact of attempting to use the ERA-I profile anomalies, rather
than retrieved profile anomalies, is presented. The end result show conclusively that we did need to retrieve the true profile
anomalies, using ERA-I profile anomalies, for example, results in increased errors in the trace gas retrievals.

4.2   Channel Selection

225 As discussed in Section 2 only channels that remain A+B throughout the mission are used, noting that the designation A+B
does not apply to detectors in the M-11 and M-12 long wave detector arrays. Initial retrievals showed that the AIRS short
wave detectors are drifting slightly, so these channels are also excluded from the anomaly fits (except for demonstration tests
as discussed below). Unfortunately, the use of only A+B detectors greatly restricts the number of available channels in the
important long wave CO_2 temperature sounding region from 710-780 cm⁻¹, where many channels are either A-only or B-only.
230 It is important to weight these channels relatively strongly in the retrieval minimization. Since we also wish to de-emphasize
stratospheric contributions to the minor-gas rates only every 5th channel from 650-720 cm⁻¹ was included in the retrieval. In
addition, any channels in this range with Jacobians that peaked above 10 hPa were excluded.

All channels in the M-5 array were excluded since they have relatively poor radiometric stability (as will be shown later).
Several window channels that are sensitive to CFC11 were excluded, although many channels sensitive to CFC12 were in-
235 cluded, and CFC12 trends were retrieved. Many H_2O channels were included, since they are mostly A+B and have been stable
throughout the mission. After some experimentation, four channels sensitive to N_2O were also excluded since they appear to
be behaving significantly out-of-family. Three of these channels are located near the end of the M-4c array, which also exhibits
some anomalous frequency shifting behavior (Aumann).

A total of 470 channels remained after this pruning process. These channels are nicely distributed throughout the AIRS
240 spectrum and are easily sufficient for 1D-var retrievals. The nominal number of DOFs for tropical scenes for this channel set
are ~6 ozone DOFs, ~8 temperature DOFs, and 12 H_2O DOFs. The larger number of H_2O DOFs is likely due to the large
number of H_2O channels used (321 out of 470 channels).

The overall sensitivity of the anomaly retrievals to CO_2 is shown is shown in Figure 6 where the mean CO_2 Jacobian,
averaged over all channels, is plotted. The CO_2 sensitivity peaks around 400 hPa, and drops to near zero at the surface. There
245 is some dependence on stratospheric CO_2, but stratospheric CO_2 trends, especially in the lower stratosphere, should track the
tropospheric trends, albeit with growth rates that are slightly influenced by previous years due to age-of-air. This figure also

shows the mean CO_2 Jacobian is all channels below 700 cm^{-1} are removed (all sensitive to the stratosphere). Retrieval tests using this restrictions are discussed later.

4.3 Temperature and Minor Gas Jacobian Co-linearity

250   A non-standard "correction" is made to the minor gas retrievals that attempts to correct for the co-linearity of the temperature and minor gas Jacobians. CO_2 retrievals using hyperspectral infrared are difficult because of this co-linearity. As stated above, the ERA-I model fields are matched one-to-one with each clear observations, followed by a RTA computation of a simulated radiance, using constant amounts of minor gases throughout the mission. Since the ERA-I spectral anomalies are very similar to to observed AIRS anomalies, we can partially evaluate the effect of the Jacobian co-linearities by retrieving the minor gas

255   amounts from the ERA-I simulated anomalies that contain no minor gas variations. We illustrate this with CO_2 retrievals in Figure 7.
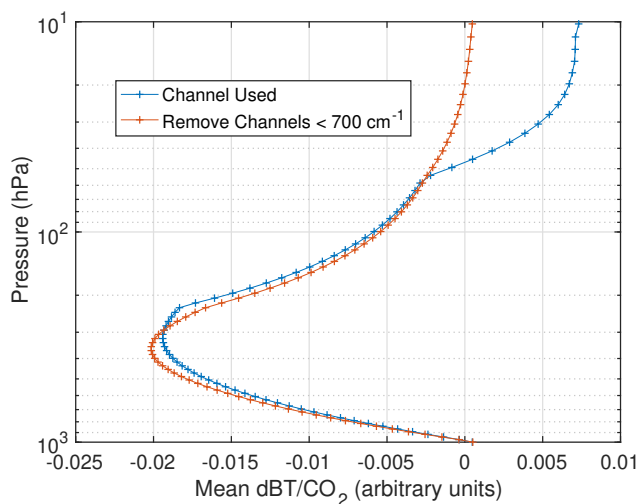
Figure 6. Mean of CO_2 Jacobians for all channels used in the anomaly retrievals, and the same if all channels below 700 cm^{-1} (stratospheric channels) are excluded.

While the long-term trends are not very sensitive to this removal of co-linearity, the lowered noise this approach affords is extremely useful for detecting and understanding shifts in the AIRS radiometry due to various instrument shutdowns that occurred over the mission.
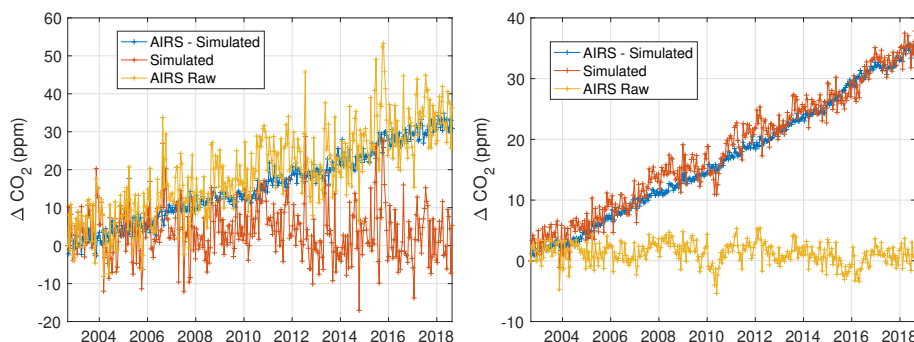
Figure 7. Illustration of "noise" removal in the CO_2 anomaly retrievals by subtracting the CO_2 retrieved from ERA-I simulations from the observed CO_2 retrievals. Left: -55° latitude CO_2 retrieval. Right: ± 50° latitude average CO_2 retrieval.

5 Anomaly Retrievals

5.1 AIRS Events

Evaluation of the anomaly retrievals requires some knowledge of the AIRS mission events. Table 1 summarizes the major events during the AIRS mission that had thermal consequences for either the spectrometer or the focal plane arrays. While most of these events were minor, recent measurements of the AIRS frequency shifts (Aumann) highlight that these events are associated with small shifts in the AIRS frequency scale. These shifts are indicative of very small movements of the detectors relative to the instrument spectrometer axis, and therefore they could also affect the absolute radiometry because viewing angles to the Earth and cold scenes might change every so slightly. We will refer to these events during discussions of the anomaly retrieval results.

Table 1. Summary of AIRS events that had a thermal impact on either the spectrometer, the focal plane, or both.

Date	Event
10/29/03	AQUA shutdown lasting for several weeks (solar flare)
01/09/10	Single event upset, focal plane temperature cycling
03/28/14	Single event upset, small focal plane cooler variation
09/25/16	Single event upset, one cooler restart

5.2 Truth Anomalies

The retrieved minor gas anomalies are compared to the NOAA Earth System Research Laboratories (ESRL) monthly mean data derived from in-situ measurements (Tans and Keeling). We chose the ESRL Mauna Loa, Cape Grim, and Global mean data for CO_2, N_2O, and CH_4. Monthly anomalies for these in-situ datasets were computed using the same methods used to compute the BT anomalies for consistency. We focus mainly on the global CO_2 ESRL anomalies since they are derived from a

wide geographical range and sites and carefully merged to avoid local sources. The N_2O ESRL anomalies provide information
on AIRS channels in the 1250 -1310 cm^{-1} region that are distinct from the main CO_2 channels below 780 cm^{-1}. (There are also
strong N_2O channels in the short wave band of AIRS.) The CH_4 anomalies mostly probe AIRS channels from 1230 to 1360
cm^{-1}. There is some concern that CH_4 anomaly trends may have more spatial variability than CO_2 and N_2O, however we find
good overall agreement with the ESRL global CH_4 trends, and CH_4 provides some sensitivity to channels that overlap with
N_2O, but extend a bit further into the water band.

We focus mostly on the use of CO_2 for AIRS stability estimations since CO_2 is so well measured and has the largest BT
signal in the AIRS spectrum (relative to N_2O and CH_4). In addition, the N_2O and CH_4 spectra overlap strongly in the AIRS BT
spectrum, possibly introducing some retrieval uncertainty relative to CO_2. Absolute errors in the ESRL CO_2 data are estimated
to be ~0.2 ppm (https://www.esrl.noaa.gov/gmd/ccl/ccl_uncertainties_co2.html), with yearly growth rate uncertainties of ~0.07
ppm/year (https://www.esrl.noaa.gov/gmd/ccgg/trends/gl_gr.html). Anomaly growth rate errors averaged over 16 years are
likely much lower since yearly sampling errors should diminish over time. Moreover, most absolute errors will not be applicable
to the CO_2 anomaly, which is a relative measurement. Therefore it is difficult to definitively estimate the ESRL anomaly trend
uncertainty. If the yearly growth rate uncertainties of 0.07 ppm/year are random, then the average of 16 of these growth rates
would be 0.018 ppm/year, which corresponds to a percentage uncertainty of 0.8% in the anomaly trend.

Estimates for N_2O and CH_4 anomaly trend uncertainties using the ESRL stated uncertainties in yearly growth rates, and
assuming these are random errors each year, are 3.5% and 2.4%. These larger uncertainties, and the smaller total impact of
these two gases on the AIRS BT anomalies, suggest that the best estimates for AIRS stability are likely derived from the CO_2
anomalies.

5.3 Short Wave Trends

Most of the anomaly retrievals performed here only included AIRS channels in located below 1615 cm^{-1}, avoiding the short
wave channels in the 2181 to 2665 cm^{-1} region. Early retrievals showed that the AIRS short wave channels exhibit a positive
trend compared to the longer wave channels. Moreover, anomaly fits to just the short wave channels return SST trends that are
significantly larger than both the long wave channels and both the ERA-I (OSTIA) and OISST SST products.

The behavior of the AIRS short wave channel relative to the long wave is easily seen in the anomaly retrieval fit residuals.
Figure 8 shows the mean value (taken over the 365 16-day time steps for ± 30º latitude) for the residuals. All AIRS L1c
channels are plotted, which includes many bad channels, and channels that do not exist but are filled during L1c creation.
The channels selected for the anomaly fits (see Sect. 4.2) are shown in red circles. The fit residuals for channels used in these
retrievals are almost all well below 0.02K. However, the short wave channels show anomalies inconsistent with the long wave
of up to ~0.07K in the window channels past 2450 cm^{-1}.

The anomaly retrievals can respond to drifts/offsets in the AIRS radiances by retrieving geophysical variables (CO_2, tem-
perature, etc.) that vary incorrectly in time. Alternatively, un-physical changes in the radiances could also be reflected in larger
non-zero fit residuals. This could happen when the forward model Jacobians cannot model time-dependent radiance errors,
especially for jumps in the radiometric calibration that happen due to AIRS events (shutdowns). One way to examine this
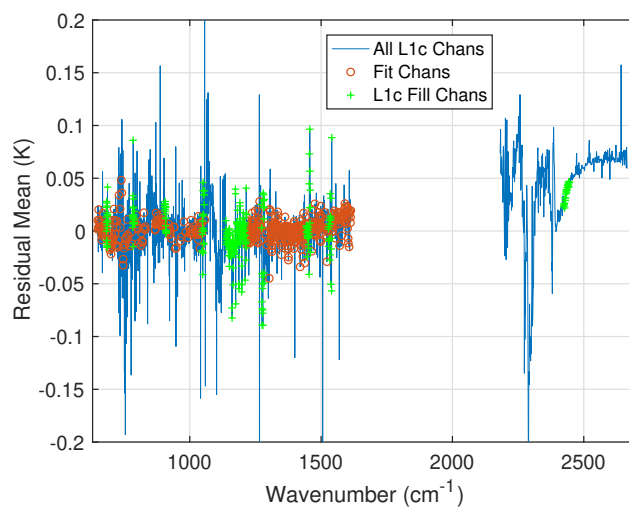
Figure 8. Anomaly fit residual, averaged over all 365 16-day time steps for ± 30° latitude. The L1c fill channels have no L1b counterparts and are simulated in the production of L1c. Note the offset in the short wave.
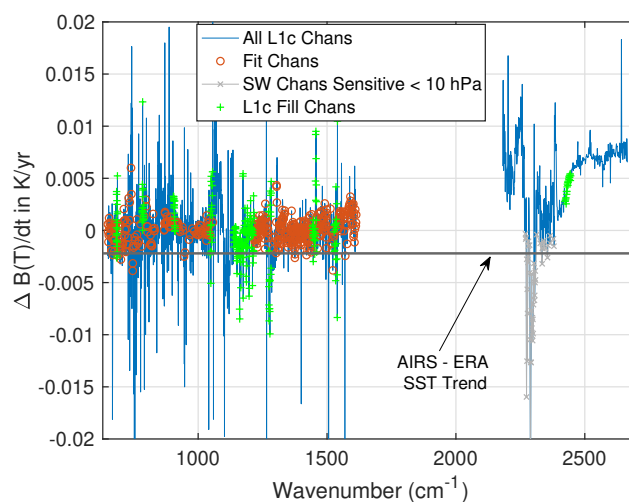
Figure 9. Linear trends in the anomaly fit residuals, averaged over all 365 16-day time steps for ± 30° latitude. Note the linear trend in the short wave in these fit residuals. Also shown is the trend difference (ERA-I SST - AIRS SST) for these data.

possibility is to look for any remaining trends in the anomaly fit residuals. These are shown for the same data set used in Fig. 8 in Fig. 9. Most of the channels used in the anomaly fits have residual slopes below 0.002K/year, although careful examination

310 of the residual time series for particular channels can exhibit jumps associated with AIRS shutdowns.

The main observation in Fig. 9 is a clear positive trend in the short wave relative to the longer wave channels used in the retrievals. The (AIRS - ERA) SST trend plotted as a solid horizontal line in this figure (discussed in Sect. {sec:sst}) shows that the AIRS short wave trends are more different from the ERA-I SST trends than the long wave channels. Most of the short wave channels, including those in the mid-troposphere, exhibit positive trends relative to the long wave, except for some channels

315 that are peaking very high in the stratosphere, below 10 hPa, that are marked in gray.

Consequently, unless otherwise noted, all the remaining results presented here use avoid the short wave channels, and use the channel set (470 channels) denoted in these figures.

5.4 CO_2 Anomaly Retrievals
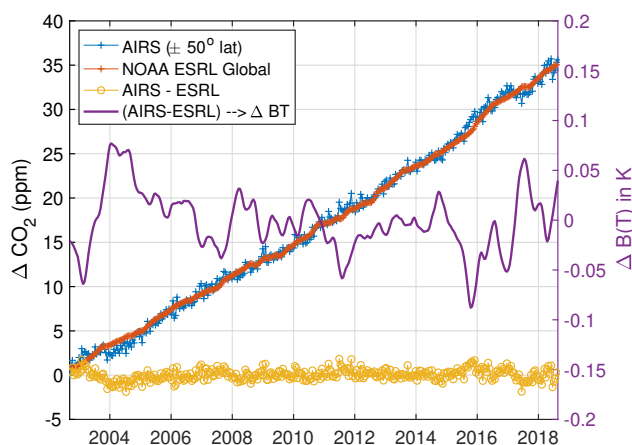
Figure 10. Retrieved CO_2 anomalies compared to ESRL global in-situ data. The CO_2 anomaly difference between AIRS and ESRL is shown in yellow. The magenta curve is that difference converted into BT units.

Figure 10 shows the retrieved CO_2 anomalies averaged over ± 50° latitude in blue and the ESRL global anomaly product in

320 red. The correspondence over time is excellent. The AIRS minus ESRL anomaly differences are shown in yellow.

In order to convert the variation in the gas anomalies to an equivalent AIRS BT anomaly temperature we computed anomaly retrievals with the observed AIRS BT anomaly spectra modified by a 0.01K/year ramp, for all channels. This 0.01K/year ramp is divided by the resulting changes in the CO_2 anomaly linear trends (ppm/year) to obtain the sensitivity of the retrieval to a trend in the AIRS radiances, in K/ppm. For CO_2 this sensitivity is 0.073K/ppm. This is about 2X larger than the largest

325 column Jacobians in the AIRS spectra, which have a value of ~0.030K/ppm. This is not unexpected, since the CO_2 column measurement is partially a relative measurement, especially for weak CO_2 channels in the window region where the absolute BT errors are mostly accounted for by (incorrect) adjustments in the SST that minimize the effect of the 0.01K/year applied
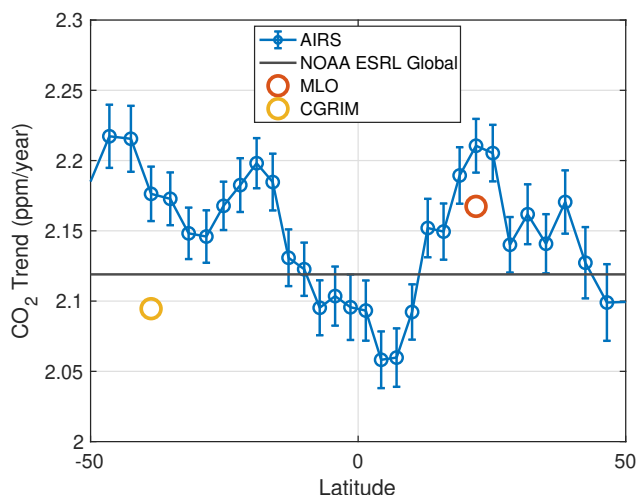
Figure 11. Observed linear trend in the AIRS CO_2 anomalies versus latitude, compared to NOAA ESRL Mauna Loa (MLO), ESRL Cape Grim (GCRIM), and the ESRL global CO_2 product trends (black line).

ramp. It is also possible that the temperature profile could also adjust to minimize sensitivity of the ramp on the CO_2 ppm values. In addition, this sensitivity estimate assumes all AIRS channels are drifting, which is clearly an approximation given

330 the results shown here.

Table 2. Slope of the (AIRS - ESRL) CO_2 anomalies in ppm/year units.

Data Set CO_2	Mean Trend Difference (ppm/year)	Uncertainty in Trend (ppm/year)
Global	0.032	0.012
Mauna Loa	0.033	0.023
Cape Grim	0.056	0.020

The magenta curve in Fig. 10 is the (AIRS minus ESRL) anomaly differences converted to BT units using the 0.073K/ppm sensitivity factor. This curve has been slightly smoothed for clarity. The right-hand side vertical axis shows the variations in this curve in BT units. Most of the BT variability is within ± 0.05K, however a transition in BT in late 2003 is larger. This larger transition is likely due to the Nov 2003 shutdown of the AQUA spacecraft. The AIRS channel center frequencies were

335 shifted due to this shutdown (Strow et al., 2006) and were subsequently corrected in the AIRS L1c product (Aumann; Manning et al., 2019). In addition, as reported in (Strow et al., 2006) interference fringes in the AIRS entrance filters shifted after the Nov. 2003 AQUA shutdown because AIRS was restarted at a slightly different spectrometer temperature. The fringes change the AIRS spectral response functions, which has not yet been corrected in the AIRS L1c product radiances.

Figure 11 illustrates the differences between the AIRS and ESRL CO_2 growth rates. The growth rate were computed using

340 Eq. 1 where the input data is the CO_2 ppm anomaly rather than a radiance. Figure 11 shows the a_1 term in this equation,

computed as a function of latitude. The CO_2 growth rates are not completely uniform from year-to-year, so Eq. 1 cannot perfectly fit the trend data. However, it provides a convenient metric for inter-comparing these two CO_2 anomalies. Note that the error bars shown for AIRS are slightly over-estimated because of the fact that Eq. 1 does not perfectly fit the slightly non-linear anomaly curve. The error estimates are for 95% confidence intervals and have been lag-1 auto-correlation corrected

345   using the approach detailed in (Santer et al., 2000).

The Mauna Loa and Cape Grim growth rates are also shown, also derived using Eq. 1, as is the ESRL global rate, indicated by the dark black horizontal line. If the 16-year in-situ rates indeed have an estimated error of 0.018 ppm/year (assuming the 0.07 ppm/year uncertainties in the ESRL rates are random), then AIRS is in close agreement with ESRL averaged over latitude. The latitude dependence of the AIRS derived rates appear to have clear latitudinal dependencies, with lower rates near

350   the ITCZ and higher rates in regions of descending air. We do not examine this latitude dependence in this work, not only is it small, it could also be related to small inaccuracies in our retrieval algorithm.

Table 3. Slope of the (AIRS - ESRL) CO_2 anomalies in K/Decade units. Trend differences for various modifications of our retrieval algorithm are shown, see the text for details. Note that Baseline is the algorithm configuration detailed in the text and used for inter-comparisons.

CO_2 Test	Mean Trend Difference (K/Decade)	Uncertainty in Trend (K/Decade)
Global		
Baseline	-0.023	0.009
No Strat	-0.034	0.008
No Cov Reg.	-0.043	0.009
No ν Cal.	-0.059	0.010
Shortwave Only	+0.070	0.009
ERA-I T(z)	+0.060	0.035
Mauna Loa		
Baseline	-0.024	0.017
Cape Grim		
Baseline	-0.040	0.020

Since the CO_2 growth rate measurements are not sensitive to year-to-year variability in the CO_2 anomaly, we instead use the (AIRS - ESRL) global anomaly differences shown in Fig. 10 to quantify the AIRS stability. Any linear trend differences between the AIRS and ESRL CO_2 in Fig. 10 are quantified by fitting the (AIRS - ESRL) CO_2 anomaly differences to Eq. 1.

355   Table 2 summarizes any trend in AIRS relative to ESRL by tabulating the a_1 terms from the fit for the ESRL global, Mauna Loa, and Cape Grim sites. The uncertainties are as before, 95% confidence intervals corrected for lag-1 auto-correlations. As one might expect, the global trends agree the best, and Cape Grim the worst. The higher errors for Cape Grim may be related to our clear subset having fewer samples at -40º latitude relative to the 20º latitude zone occupied by Mauna Loa. These mean differences are extremely small, corresponding, for global, to 1.5 ± 0.6% trend differences.

360   Table 3 shows the conversion of the CO_2 ppm trend differences to equivalent BT differences using the 0.073 K/ppm sensitivity conversion. The baseline entry, first line of the table, represents the final configuration for the anomaly retrievals and represents our best estimate for the true differences between the ESRL and AIRS CO_2 anomaly trends, namely -0.023 ± 0.009 K/decade. This is an exceedingly small trend difference. While suggesting that AIRS is extremely stable, for channels sensitive to CO_2 and temperature, systematic errors may be larger than the differences reported here. Our optimistic estimate of the ESRL

365   global anomaly uncertainty, 0.8%, is equivalent to 0.017 ppm/year or 0.27 ppm over 16 years. From Table [tableco2ppm] the AIRS minus ESRL global trend differences are about 2X times this optimistic estimate for the ESRL uncertainty. This translates, in Table 3 to an estimate for AIRS stability of -0.023 ± 0.009 K/decade.

     In addition to the possible 0.8% uncertainty in the ESRL global trends, our AIRS anomaly retrieval could be in error if the CO_2 Jacobians are inaccurate. The HITRAN database (Gordon et al., 2017) reports uncertainties in the CO_2 line strengths of

370   1-2%. These uncertainties would translate into the same percentage error in the Jacobians. In addition, atmospheric spectra are sensitive to line widths, line shape, line mixing, often at temperatures that are not measured in laboratory spectra. Characterizing the combination of these errors is essentially impossible, so here we assume a 1% uncertainty in the CO_2 Jacobians, using the line strength uncertainty only. If the ESRL 0.8% uncertainty is combined in quadrature with the 1% HITRAN uncertainty, a total minimum expected uncertainty in the CO_2 anomaly trends is 1.3%. This translates to a BT uncertainty of 0.02 K/decade,

375   close to our mean trend difference between AIRS and ESRL based on the CO_2 anomaly measurements. This may be a more accurate uncertainty estimate for this measurement rather than the 0.009 statistical uncertainty derived from fitting the AIRS minus ESRL anomalies.

     Table 3 also shows the results of a number of fit testing the sensitivity of the retrievals to various retrieval alternatives. The "No Strat" entry removed all channels that primarily sense the stratosphere by removing all channels below 700 cm^{-1}. Fig. 6

380   shows how this modifies the mean CO_2 Jacobian used in the retrieval, essentially removing all sensitivity to CO_2 above 60 hPa. Unfortunately channels above 700 cm^{-1} have some residual sensitivity to CO_2 in the stratosphere, and removing channels below 700 cm^{-1} may make it more difficult to properly minimize the retrieval residuals for some channels above 700 cm^{-1}. If S_a is completely removed, removing a-priori profile regularization, the CO_2 anomaly trend difference increases by a factor of two. Removing the L1c frequency calibration adjustments increases the anomaly trend differences by nearly a factor of three,

385   and changes their sign. If only short wave channels are fit (excluding channels that peak above 10 hPA, and some channels sensitive to both carbon monoxide), the mean trend differences are more than three times larger than the baseline, again with a sign change.

     The last test, labeled "ERA-I T(z)", examines the impact of performing simultaneous retrievals of temperature profiles while retrieving the CO_2 anomalies by using the ERA-I temperature profiles anomalies instead of fitting for them. This test increased

390   the anomaly differences between AIRS and ESRL by almost a factor of three, with a significant increase in the uncertainty of the trend, giving 0.35 K/decade instead of close to 0.009 K/decade for the baseline.

     Table 3 also shows the Mauna Lao anomaly difference, which is close to the global result, although accompanied by a higher uncertainty of 0.017 K/decade compared to the 0.009 K/decade for the global anomaly. Cape Grim anomaly differences are
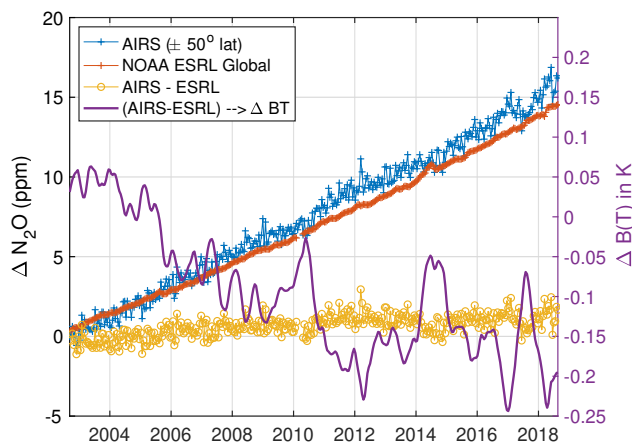
Figure 12. Retrieved N_2O anomalies compared to ESRL global in-situ data. The N_2O anomaly difference between AIRS and ESRL is shown in yellow. The magenta curve is that difference converted into BT units.

almost two times higher than the global trend differences, but this is not surprising given the much lower number of observations

395 at that latitude.

The retrieved AIRS global CO_2 anomalies did detect a small seasonal pattern in the anomaly for latitudes above 40° N of with an amplitude of ~0.5 ppm. This is due to the residual of the seasonal cycle of CO_2 that is not completely removed when constructing the BT anomalies.

Table 4. Slope of the (AIRS - ESRL) N_2O anomalies in K/Decade units.

Data Set N_2O	Mean Trend Difference (K/Decade)	Uncertainty in Trend (K/Decade)
Global	-0.141	0.012
Mauna Loa	-0.200	0.030
Cape Grim	-0.080	0.033

Note that radiometric shifts or drifts in the AIRS BT time series could be either reflected in incorrect geophysical trends, or

400 partially buried in the anomaly fit residuals. The high quality of the anomaly retrievals for CO_2 and the small fit residuals for CO_2 channels strongly suggest that the AIRS blackbody is extremely stable, at least for long and mid wave A+B channels. The SST retrievals discussed later reinforce this conclusion. However, we do see evidence of radiometric shifts due to discrete AIRS events (especially for N_2O and CH_4) that might be amenable to correction. Future work will include careful examination of both the anomaly retrievals and their residuals, likely in an iterative fashion, in order to determine what channels are responsible

405 for unphysical shifts in the anomaly products.

5.5 N$_2$O Anomaly Retrievals

The N$_2$O retrieved anomaly time series is shown in Fig. 12. Clearly the observed N$_2$O anomaly is growing slightly faster than the ESRL values. The N$_2$O anomalies are converted to equivalent BT variations just as for CO$_2$, but with a derived sensitivity of 0.140 K/ppb. Table 4 tabulates the derived trend for the (AIRS minus ESRL) anomaly by fitting the difference to Eq. 1, and

410 then converting to BT units. The trend differences here are much larger than for CO$_2$. Examination of either the AIRS minus ESRL anomalies in ppb, or their equivalent in BT units (left hand y-axis) suggest that two unphysical steps might be present in the time series, one in mid-2005 and another on in mid-to-late 2010. Unfortunately, these steps do not closely coincide with AIRS events, possibly appearing more than one year after the Nov. 2003 event and and slightly less than one year after the Jan. 2010 event.
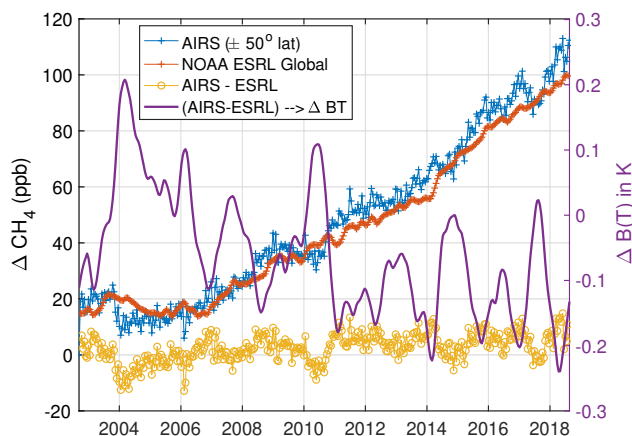
Figure 13. Retrieved CH$_4$ anomalies compared to ESRL global in-situ data. The CH$_4$ anomaly difference between AIRS and ESRL is shown in yellow. The magenta curve is that difference converted into BT units.

Table 5. Slope of the (AIRS - ESRL) CH$_4$ anomalies in K/Decade units.

Data Set CH$_4$	Mean Trend Difference (K/Decade)	Uncertainty in Trend (K/Decade)
Global	-0.107	0.024
Mauna Loa	-0.062	0.039
Cape Grim	-0.100	0.037

415   To illustrate the effect of these two discrete shifts on the anomaly trend differences we empirically introduce a step in our retrieved N$_2$O time series of -0.6 ppb on July 1, 2005 and another step on Jan. 18, 2010 of -0.5 ppb. The trend difference between this empirically modified time series and ESRL, in BT units, becomes -0.022 ± 0.009 K/decade, very similar to the CO$_2$ trend differences. The main point of this exercise is to illustrate that just two two small discrete radiometric shifts could be responsible for the higher trend differences between AIRS and ESRL for N$_2$O. More work is needed to map these discrete

420   non-physical events in the retrieved N_2O anomaly time series back into steps in the AIRS BT time series. The hope is that careful examination of the anomaly time series residuals during this process would highlight specific channels (or cluster of channels) that are behaving non-physically.

5.6   CH$_4$ Anomaly Retrievals

The CH$_4$ retrieved anomalies have some similarities to the N_2O anomalies, since the spectra of both gases occur in the same
425   general spectral region. Figure 13 shows the CH$_4$ results using the same approach as for CO_2 and N_2O. The ppb to BT conversion for CH$_4$ was measured to be 0.023 K/ppb, significantly lower than for CO_2 or N_2O, although total BT trend due to CH$_4$ is only marginally lower than CO_2 and N_2O.

The high variability of atmospheric CH$_4$ growth is well known, as can be seen in the ESRL curve in Fig. 13. The AIRS derived anomalies follow that variable growth rate quite nicely overall. It should be noted that the ESRL CH$_4$ curve is more
430   variable than CO_2 and N_2O, and may be less uniform globally, making CH$_4$ a less ideal gas for testing AIRS stability. However, the AIRS minus ESRL anomaly differences are valuable in that they, like N_2O, highlight discrete jumps that can often be identified with AIRS events, such as late 2003 (biggest jump), early 2010, and possibly in early 2014. The positive jump in the CH$_4$ anomaly difference near March 2014 also coincides with a jump in the N_2O anomaly difference, both taking place after the March 2014 event. However, this apparent jump seems to fade within one year for both gases. We believe this might be
435   caused by AIRS frequency shifts that occurred in the M-4a and M-4c detector modules after this event. Those frequency shifts appeared to disappear within one year, and at present they are not corrected for in the AIRS L1c product.

Table 5 lists the trend differences between AIRS and ESRL for CH$_4$, showing trends differences that similar to those for N_2O, presumably since both gases occur in the same spectral region.

5.7   SST Retrievals

440   The SST anomaly retrievals are compared to the ERA-I supplied SST (mostly OSTIA) and to NOAA's OISST operational SST product. Although both of these SST products are tied to the ARGO floating buoy network, they are gridded SST products using interpolation derived from satellite data such as AVHRR.

A recent study (Fiedler et al., 2019) compared various SST products to the buoy network and found differences for OSTIA of 1.1 mK/year, and 7.8 mK/Year for OISST. This establishes a rough estimate of the differences in these products when
445   evaluating them relative to our retrieved SST anomalies.

Figure 14 plots time series of our retrieved SST anomaly and the co-located ERA-I SST (mostly OSTIA) anomaly, averaged over $\pm$ 30° latitude, where these products are expected to be most accurate since most buoy's are located in the tropics. The AIRS and ERA-I 16-day averaged anomalies agree very closely, their difference is shown in black. A zoom of the AIRS minus ERA-I SST is shown in Fig. 15 to highlight their differences. Steps in these differences are possibly evident near the end of
450   2003 and especially near the end of September 2016 when AIRS had an cooler-restart.

Table 6 summarizes the AIRS minus (ERA-I and OISST) anomaly trend differences, computed using Eq. 1. The trend differences are quite small for both SST products. The (AIRS minus ERA-I) trend has the same magnitude as the trend derived
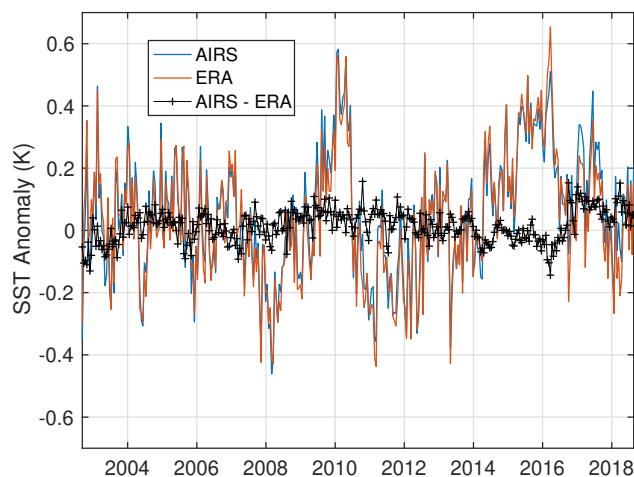
Figure 14. Tropical (± 30°) SST anomalies retrieved from AIRS compared to the ERA-I anomalies. The black curve is the difference between the AIRS and ERA-I anomalies.
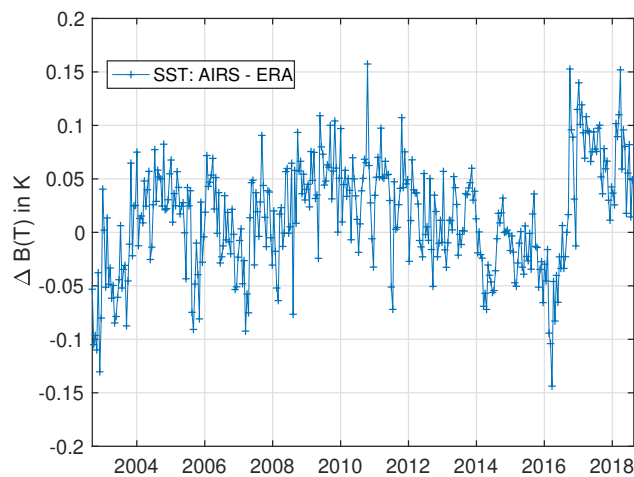
Figure 15. Zoom of Fig. 14 that highlights the shift in the AIRS - ERA-I SST anomaly presumably due to the AIRS Sept. 25, 2016 cooler restart. A small shift is also seen at the date of the Nov. 2003 AQUA shutdown.

using CO_2, but with the opposite sign. Overlap of the CO_2 and ERA-I SST within their stated uncertainty estimates is missed by 0.01K/decade, which is very small. The CO_2 and OISST trend estimates miss overlap by slightly more, 0.02K/decade.
455   However, this overlap difference is small compared to the differences between OISST and the buoy network reported by (Fiedler et al., 2019).

   Overall the excellent agreement of these two extremely independent assessments (CO_2 versus SST) to within 0.02K/decade is very encouraging given the complexity of the CO_2 measurement and the uncertainties in the SST product trends.

Table 6. Slope of the (AIRS - (ERA/OISST)) SST anomaly differences.

Data Set	Mean Trend Difference (K/Decade)	Uncertainty in Trend (K/Decade)
(AIRS - ERA-I)	0.022	0.012
(AIRS - OISST)	0.034	0.021

   Aumann (Aumann et al., 2019) recently compared the 1231 cm^{-1} AIRS channel trends to RTGSST, a precursor to OISST.
460   He used a statistical approach to remove trends in water vapor that affect the 1231 cm^{-1} channel radiances, which he concedes could introduce artifacts if there is a shift in the mean vertical distribution of water vapor. Our approach does not contain this limitation in principle, although we have not carefully examined the retrieved water vapor trends, mainly because there is no truth for comparison. An intercomparison of our results to his are not strictly possible since we used different SST products for truth and our SST anomalies used many channels. However, the trend of the 1231 cm^{-1} channel in our retrievals can be
465   derived by adding the slope of our fit residual for the 1231 cm^{-1} channel (-0.7 mK/year) to our derived SST trends for ERA-I and OISST. Using Aumann's units of mK/year, the result is a trend of 1.5 mK/year and 2.7mK/year for ERA-I and OISST respectively, with respective uncertainties of 1.2 and 2.1 mK/year. These two trends compare favorably with Aumman's night trend for 1231 cm^{-1} of +2.9 ± 0.4 mK/year. It is interesting that our OISST trend differences agrees more closely with his RTGSST trend difference since these two data sets have similar heritage. Of course the extremely low statistical errors reported
470   by Aumann do not allow overlap of these two results, but that is not necessarily expected since we use different SST products. Agreement for AIRS radiometric trends at the several mK/year level for at least a single channel should be considered quite remarkable.

   We also derived AIRS minus (ERA-I, OISST) SST trend differences using AIRS short wave only anomaly retrievals. For tropical latitudes, ± 30°, the (AIRS - ERA-I) trend is 0.078 ± 0.040 K/decade and 0.065 ± 0.09 K/decade for OISST. These
475   represent significantly higher trend than observed using long and mid wave channels only. The trend difference between (AIRS long wave minus AIRS short wave) anomaly fits is -0.058 ± 0.026 K/decade, clearly indicating the short wave positive drift relative to the long wave.

   The latitude dependence of the AIRS derived SST trends versus ERA-I and OISST may eventually help determine the source of some of these differences. Figure 16 shows these trends between ± 60° latitude. The uncertainties in these trends are
480   ~0.005K/year, but are not shown since these uncertainties are primarily geophysical in nature (how linear is the SST trend) and

affect each SST product identically. Agreement is quite good among all products in the northern hemisphere, while OISST is systematically lower than AIRS and ERA-I in the southern hemisphere. Also shown are the AIRS SST trends using only the short wave channels (gray curve), which are always higher than the long wave AIRS trends except at the highest latitudes and near the equator.

485   Unfortunately, the AIRS Level 2 retrieval algorithm only uses short wave channels for surface temperature retrievals (Susskind et al., 2014). A recent inter-comparison of surface temperature trends from the AIRS Level 2 retrievals to three established surface temperature climate products (Susskind et al., 2019) concluded that the AIRS surface temperature trends were 0.24 K/decade, slightly higher than GISTEMP's (Hansen et al., 2010) value of 0.22 K/decade, and significantly higher than the HadCRUT4 (Morice et al., 2012) and Cowtan and Way (Cowtan et al., 2015) values of 0.17 and 0.19 K/decade respectively.

490   The results presented here conclude that the AIRS short wave channels are drifting positive by about 0.058 K/decade relative to the long wave channels, which appear to be in extremely good agreement with established SST climate products as discussed above. If we subtract this 0.058 K/decade AIRS short wave drift from the the AIRS 0.24 K/decade trend presented in (Susskind et al., 2019) we obtain a corrected AIRS trend of 0.18 K/decade, much more in line with the HadCRUT4 and C+W values. In this case GISTEMP is now the only outlier. A more straightforward way to validate the reported AIRS Level 2 surface trends
495   reported by (Susskind et al., 2019) would be to directly compare them to other SST products such as OISST, but unfortunately this was not part of the (Susskind et al., 2019) analysis.
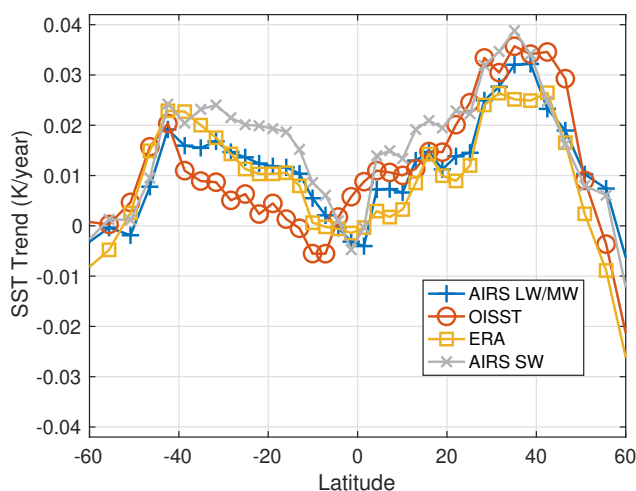
Figure 16. Latitude dependence of the linear trend in the AIRS retrieved SST, OISST, and ERA-I SST. Also shown are the SST trends when only the AIRS short wave channels are used to compute the anomalies.

5.8 CFC12 Retrieval

All anomaly retrievals presented here included CFC12 retrievals. Although these are not used for quantitative assessments of AIRS radiometric stability, the retrieved CFC12 anomaly is shown in Fig. 17 for completeness. Excellent agreement between

500   the AIRS observed CFC12 and the ESRL Northern Hemisphere measurements (ESRL). The linear trends derived from these

two curves are -2.94 ± 0.04 ppt/year for AIRS, and -2.93 ± 0.02 ppt/year for ESRL, nearly perfect agreement. These results

give us confidence that the SST retrievals have not been compromised by CFC12 contamination, since there are a number of

channels sensitive to both. Note that the trend of ~40 ppt of CFC12 derived here from AIRS is equivalent to only ~0.11K in

BT!
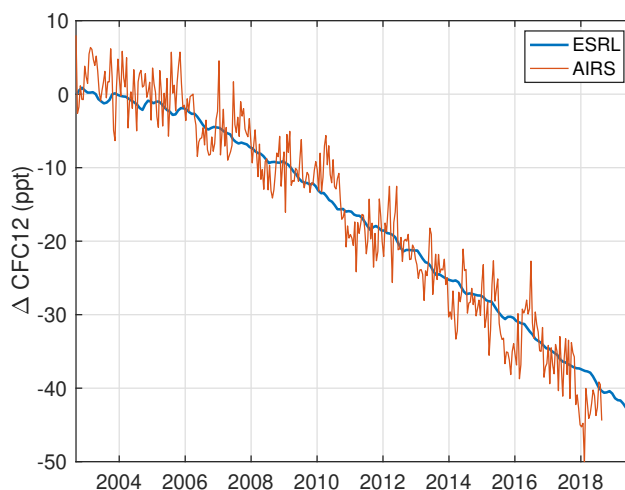
Figure 17. AIRS CFC12 retrieved anomaly compared to the NOAA ESRL Northern Hemisphere anomaly. Note that a 40 ppt trend in CFC12 corresponds to about 0.11K in brightness temperature for the channel with the highest CFC12 Jacobian.

6   Retrieval Residuals

The anomaly fit residuals provide a wealth of information on the behavior of each AIRS channel versus time. As stated earlier,

unphysical shifts in the AIRS radiance time series can be reflected in either the retrieved geophysical anomalies or in the fit

residuals. Jumps in the fit residuals will generally take place when the shifted radiances cannot be "adjusted away" by the BT

Jacobians, which require a reasonably accurate physical response to radiance jumps. We believe that the anomaly retrieval

510   approach presented here will allow objective corrections to AIRS radiances, especially for radiance jumps that can be tied to

instrument events. The excellent agreement between the CO_2 and SST anomalies and in-situ data strongly suggests that the

AIRS blackbody is very stable, which is key to climate-level trend measurements.

There are several likely causes for some of the differences seen here between our observed anomalies and the N_2O and CH_4

truth anomalies from ESRL. Shifts in the frequency calibration of AIRS (Strow et al., 2006; Manning et al., 2019) have largely

515   been removed in the AIRS L1c product, although some transient shifts in the AIRS M-4a and M-4c arrays (that cover N_2O

and CH_4 channels) have not yet been corrected in L1c (see (Aumann)). The AIRS frequency shifts imply that detector views

of the blackbody and cold scene targets have also shifted during the mission. While these shifts are very small, radiometric

drifts/shifts could arise from these focal plane movements if the blackbody and cold scene targets are not perfectly uniform. As mentioned in Sec. 5.4, shifts of interference fringes in some of the AIRS entrance filters when AQUA was restarted in

520 Nov. 2003 may also contribute to the observed anomaly shifts. These fringe shifts have been modeled by the authors and future work may include modification of AIRS radiances before Nov. 2003 to remove the effects of these small shifts in the instrument spectral response function.

Here we present several views of the AIRS anomaly fit residuals as examples on how future work might proceed to potentially correct the AIRS radiances for small remaining radiometric drifts/shifts.
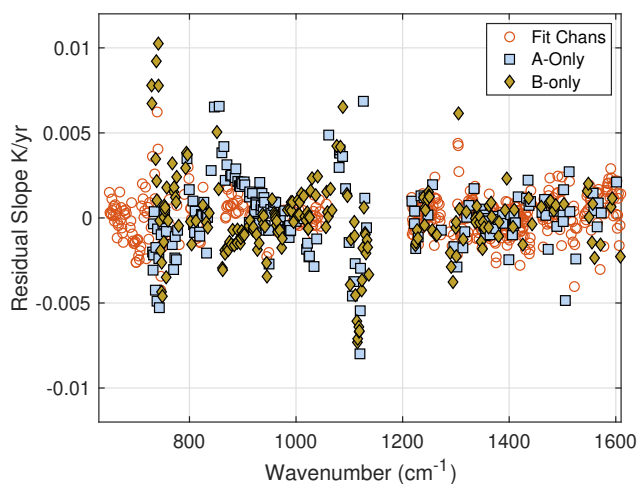
Figure 18. Slope of the AIRS anomaly residuals separated by A+B (Fit channels), A-Only, and B-Only. This illustrates trends in the A-only and B-only channels relative to A+B channels in some modules. The A-only and B-only channels were not used in the fitting, so they are not strictly residuals, but Observed - Computed differences.

525 Figure 18 shows the BT anomaly fit residual slopes for A+B, A-only, and B-only channels separately. Most of the A+B channels shown, all of which were used in the anomaly retrievals, are within ± 0.004 K/year of zero. While a large number of A-only and B-only channel are in agreement, there are a number of cases where they exhibit significant slopes (trends) that are not in agreement with the A+B channels. Module M-05 channels near 1100 cm^{-1} are clearly drifting differently than the other channels (we did not use any A+B M-05 channels in the retrievals since they are also in error). Module M-08 channels

530 near 851 cm^{-1} show a clear separation between A+B channels and A-only, B-only. Clearly, the opposite sign of the A-only versus B-only drifts are largely cancelled when A+B channels are used. Since the SST retrievals are quite good, and because the surface channels near 1200 cm^{-1} agree with the A+B channels, we conclude that the A-only and B-only drifts are real, and possibly due to drifts, or offsets, in the exact part of the blackbody and/or cold target scenes observed by these detectors.

Since the N$_2$O retrieved anomalies exhibit some small unphysical behaviors, we examine the fit residuals for the 24 channels

535 (used in the retrievals) that are most sensitive to N$_2$O. Visual inspection of these channel's residual time series clearly indicated that 12 of them had easily identifiable features due to AIRS events. Figure 19 shows three different averages of these residual

time series; (a) 12 good channels, with no strong evidence of AIRS events, (b) 12 bad channels which clearly exhibit jumps at the time of AIRS events, and (c) the mean time series for all 24 channels used in the anomaly fits. We see that the good channel mean (blue) is very flat, with a slight indication of a jump near the Nov. 2003 event. The bad channel curve (red) shows a large

540   jump near Nov. 2003, possibly some longer-term drifts, and a feature in March 2014 that seems to last for 1 to 1 1/2 years. This last feature can change sign depending on which bad channel is observed, making it very likely that this is due to the M-4a/M-4c frequency calibration shift that is not yet corrected in the L1c product.

A new set of anomaly retrievals were produced, but with the 12 bad N_2O channels removed. When compared with the ESRL N_2O anomalies, this change produced slightly better agreement with ESRL after Nov. 2013. The slope of the (AIRS

545   - ESRL) anomaly difference curve was reduced from -0.141 K/Decade (as reported in Table 4) to -0.113 K/Decade, a slight improvement. This drift relative to ESRL reduces to -0.069 K/Decade if anomaly data before Nov. 2013 is ignored. This illustrates that improvements to the AIRS products can be improved by removing channels with residuals that have non-physical jumps. If the Nov. 2013 radiometric jumps can be removed (whether due to frequency shifts, fringe shifts, or pure radiometric jumps) even higher stability is possible. However, one could presently begin the AIRS time series, say on Jan. 1,

550   2004 and retain a stability approximately 2X better than climate trends.

These results illustrate a simple case for how the anomaly fit residuals can be used to improve AIRS trend products. In this work we have not looked for non-physical jumps in the retrieved temperature, H_2O, and O_3 profile anomalies. These products likely exhibit some of these behaviors and need to be included in any comprehensive study to further improve the AIRS radiance stability. Some sort of iterative approach will likely be needed in order to ensure that these small remaining

555   radiometric jumps become undetectable in both the retrieved anomalies and in the anomaly residuals.
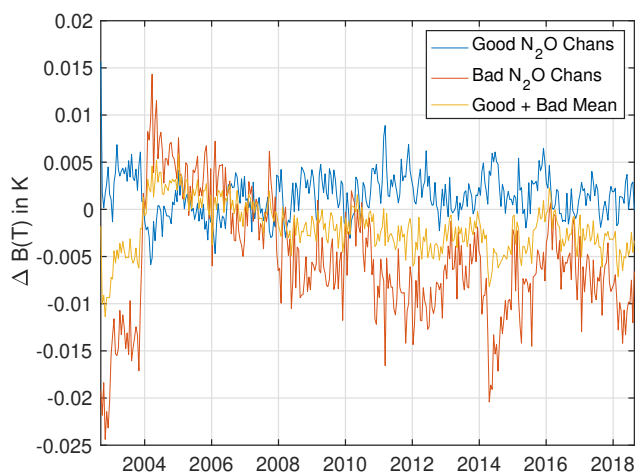
Figure 19. Anomaly fit residual time series for various combinations of 24 channels sensitive to N_2O in the long wave. The bad N_2O channels have easily visible jumps at times corresponding to AIRS hardware events.

7 Conclusions

A framework for establishing stability of the AIRS radiances has been introduced that uses retrievals of minor gas and SST trends from BT anomaly spectra. Extremely good agreement between retrieved CO_2 trends (or anomalies) and in-situ trends from NOAA ESRL illustrates that a large fraction of AIRS channels are extremely stable, well below climate trends, where

560   agreement with ESRL CO_2 anomalies is -0.023 ± 0.009 K/Decade. The SST anomaly retrievals also compare favorably to the ERA-I reanalysis and to NOAA's OISST SST product, with differences of less than 0.022 K/Decade, and slightly higher values for comparisons to OISST. Such good agreement for a wide range of detectors strongly suggests that the AIRS blackbody is very stable.

Unphysical radiometric jumps are observed in the all retrieved anomaly time series, but especially for N_2O and CH_4. These

565   jumps can largely be related to AIRS events, and we illustrate how the anomaly fit residuals, combined with inter-comparisons to truth anomaly trends such as N_2O may provide a way to correct small remaining jumps in some AIRS channels.

This work emphasizes that users of AIRS data for climate applications must pay careful attention to channel selection, since certain detector arrays and channels are presently not suitable for climate trending, including all of the AIRS short wave channels. However, establishment of such a high level of stability for so many remote sensing observations/channels is highly

570   unusual, and should lead to a high level of trust in AIRS climate trends that pay careful attention to only using validated climate-level channels.

Acknowledgement

The authors thank Steve Broberg, NASA JPL AIRS Project Office, for supplying us with a table of AIRS events. We also thank Steven Buczkowski at UMBC/JCET for the extensive data handling and production needed for this work. The hardware

575   used for this work is part of the UMBC High Performance Computing Facility (HPCF). The facility is supported by the U.S. National Science Foundation through the MRI program (grant nos. CNS-0821258, CNS-1228778, and OAC-1726023) and the SCREMS program (grant no. DMS-0821311), with additional substantial support from the University of Maryland, Baltimore County (UMBC).

Appendix A: AIRS Detector Array Wavenumbers

580   Table A1 shows the wavenumber ranges covered by each of the 17 AIRS arrays.

Appendix B: Anomaly and Profile Trend Retrievals

A complete simulated BT anomaly dataset was generated using ERA-I model fields, by matching each AIRS clear observation to ERA-I and generating a simulated radiance. This simulated dataset was used to set the regularization parameters for the profile inversions. The measurement of anomalies largely removes systematic errors in both the radiance observations (radio-

Array Name	Start ν (cm^{-1})	End ν (cm^{-1})
1a	2552	2677
2a	2432	2555
1b	2309	2434
2b	2169	2312
4a	1540	1614
4b	1460	1527
3	1337	1443
4c	1283	1339
4d	1216	1273
5	1055	1136
6	973	1046
7	910	974
8	851	904
9	788	852
10	727	782
11	687	729
12	649	682

Table A1. The wavenumber ranges covered by each of the 17 AIRS arrays.

585 metric accuracy) and in the RTA (spectroscopy errors). We believe that these two factors helped make the retrieval inversions quite stable, requiring only minimal regularization.

Since our interest is mainly in the minor-gas profile offsets we used 20 atmospheric layers for the retrievals (20 each for temperature, H_2O, and O_3), created by concatenating layers from the 100-layer atmospheric profile model in (Strow et al., 2003). This choice, coupled with our regularization, provided more layers than degrees of freedom, as desired. We found that 590 low noise of the AIRS zonally averaged 16-day anomalies (see Sect. 4.1 coupled with low bias errors in the measurement covariances allowed us to use only minimal regularization.

We first adapted Tikhonov-only first-derivative (L1-type) regularization which mostly removed obvious outliers, mostly in the higher latitudes in the stratosphere. This gave averaged linear-trend accuracies in our simulations of -0.03 ± 0.07 K/year compared to the ERA-I model field trends used to generate the anomaly data set. (This degrades to -0.05 ± 0.08 K/year if 595 the regularization is lowered by a factor of 10X.) A reasonable goal is to achieve trends in simulation accurate to 0.01K/year, averaged over the troposphere. We then added a-priori uncertainties to the temperature and H_2O profiles of 2.5K and 60% respectively. These covariances are not very restrictive given that measurement uncertainties are so low. It appears that their main impact is again for high latitudes under conditions where we have higher noise due to low number of clear samples.
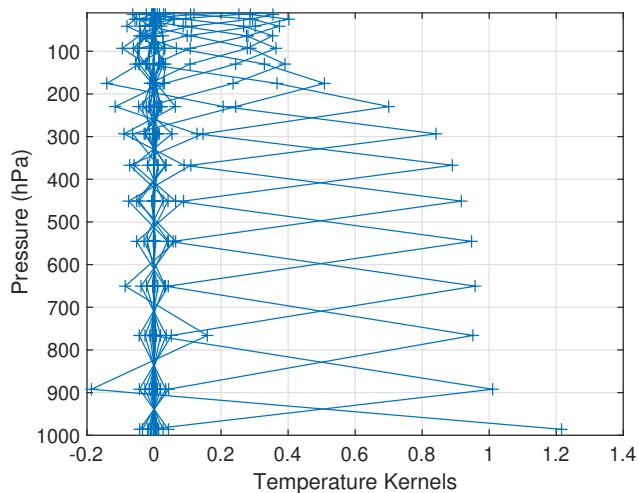
Figure B1. Temperature kernels for the anomaly retrievals. These are taken from a random day for the zonal bin centered at 28.3°N.
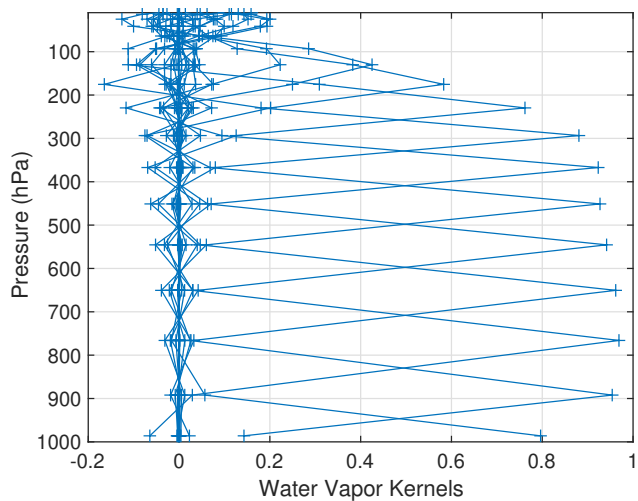
Figure B2. H_2O kernels for the anomaly retrievals. These are taken from a random day for the zonal bin centered at 28.3°N.

600   The temperature and water vapor retrieval kernels are shown in Figs. B1,B2. They exhibit a very regular spacing in the troposphere with roughly 12 well-separated kernels.
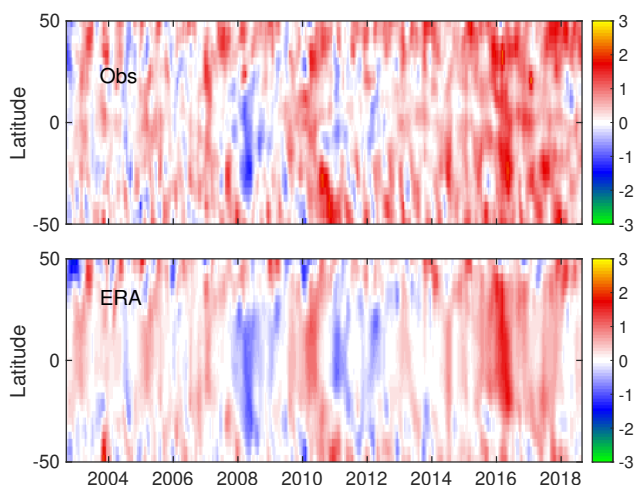
Figure B3. Retrieved 400 hPa temperature anomalies versus latitude. Top: Our retrievals from the AIRS observations. Bottom: ERA-I anomalies.

Figure B3 illustrates the 400 hPa temperatures we retrieved from the AIRS data (top panel) along with the ERA-I anomalies computed directly from the model fields. We do not expect these two data sets to compare perfectly, since for example, the ERA-I anomalies are from relatively large gridded data and the AIRS measurement are from a nominal 15 x 15 km field-of-view. Given the non-uniform sampling of our data set we do not think detailed examination of the observed versus ERA-I

605   anomalies is warranted. We do note the there are many similarities in time and latitude that give some measure of validation to our profile retrievals. Similar results are seen with water vapor profiles.
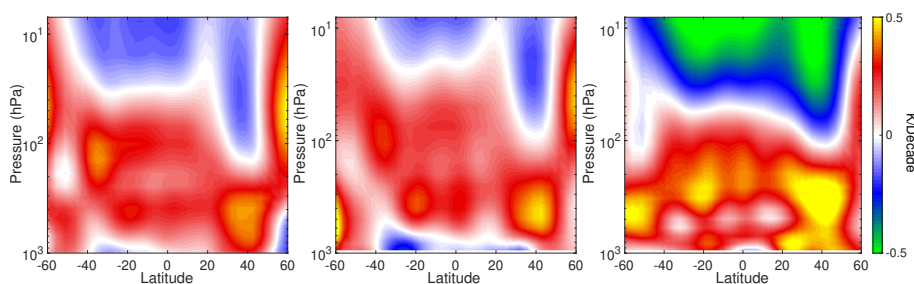
Figure B4. Temperature trends from the 16-year data period studied here. Left: ERA-I trends derived directly from the model temperature fields. Middle: Simulated retrievals of the ERA-I trends using radiance anomalies created from the ERA-I fields and our SARTA RTA. Right: Temperature profile trends retrieved from the AIRS observed anomalies. The middle panel simulation assumes that RTA is perfectly accurate.

Figure B4 summaries the temperature trend simulations and comparisons between ERA-I trends, our anomaly retrievals from the ERA-I generated radiances, and those observed with the AIRS clear subset. The trends are computed from the anomaly retrievals (or model fields) using Eq. 1, where the input is the layer temperature instead of a radiance.

610 These results have been slightly smoothed to make visual inter-comparisons easier. The left panel shows the vertical trends versus latitude directly computed from the ERA-I temperature fields. The middle panel shows our simulated temperature trend retrievals. These simulations agree quite well with the ERA-I model fields, the largest differences are seen in the lower troposphere at the higher latitudes, and near the boundary layer in the tropics. The simulated retrievals are also placing the tropopause too high, not surprising given the lack of sensitivity of the infrared to the tropopause height and our limited number

615 of vertical layers. The right panel are the temperature anomaly trends retrieved from the AIRS observed anomalies. Clearly there are significant differences between the ERA-I temperature profile trends and those we retrieved from AIRS, although the basic structure is relatively similar. Note that the uncertainties in these trends are quite high in the stratosphere (not shown) due to variations in the quasi-biennal oscillation (QBO), especially in the tropics, with errors larger than the observed trends in the vicinity of the tropopause. However, these uncertainties are largely present in both ERA-I and the AIRS observations.

620 The AIRS observed anomalies may also be impacted by errors in the BT Jacobians. The middle panel in Fig. B4 used similar RTAs for both simulations and the retrieval. The version of SARTA used for the radiance simulations is based on HITRAN2008 while the Jacobians used in the retrieval used kCARTA which is based on HITRAN2016 and a slightly modified version of CO_2 line-mixing. We expect that these spectroscopy differences have little impact since the CO_2 line strengths for the strong 15 μm bands have not changed between HITRAN versions. In addition, no noise was added to the simulated anomalies.

625 We believe that these results show that the anomaly retrievals used for measuring minor-gas trends exhibit realistic behavior and given our simulation testing this retrieval approach is likely to give accurate minor-gas trends. The impact of some of the regularization choices are discussed in Sect.5.4.

Author contributions. LLS led the study and made the comparisons between the anomaly fits and in-situ data. SDM developed the anomaly retrieval algorithm. LLS and SDM together optimized the anomaly retrieval regularization.

630 *Competing interests.* The authors declare that they have no conflict of interest.

References

Anderson, G. P., Clough, S. A., Kneizys, F. X., Chetwynd, J. H., and Shettle, E. P.: AFGL atmospheric constituent profiles (0.120km), Tech. rep., 1986.

Argo: (2019). Argo float data and metadata from Global Data Assembly Centre (Argo GDAC)., SEANOE, 2019.

635 Aumann, H.: AIRS AIRICRAD ATBD and Test Documents, https://disc.gsfc.nasa.gov/datacollection/AIRICRAD_v6.7.html.

Aumann, H. H., Chahine, M. T., Gautier, C., Goldberg, M. D., Kalnay, E., McMillin, L. M., Revercomb, H., Rosenkranz, P. W., Smith, W. L., Staelin, D. H., Strow, L. L., and Susskind, J.: AIRS/AMSU/HSB on the Aqua Mission, IEEE Transactions on Geoscience and Remote Sensing, 41, 253, https://doi.org/10.1109/TGRS.2002.808356, https://doi.org/10.1109/TGRS.2002.808356, 2003.

Aumann, H. H., Broberg, S., Manning, E., and Pagano, T.: Radiometric Stability Validation of 17 Years of AIRS Data Using Sea Sur-
640 face Temperatures, Geophysical Research Letters, 46, 12 504–12 510, https://doi.org/10.1029/2019GL085098, https://doi.org/10.1029/2019GL085098, 2019.

Banzon, V., Smith, T. M., Chin, T. M., Liu, C., and Hankins, W.: A long-term record of blended satellite and in situ sea-surface temperature for climate monitoring, modeling and environmental studies, Earth System Science Data, 8, 165–176, https://doi.org/10.5194/essd-8-165-2016, https://doi.org/10.5194/essd-8-165-2016, 2016.

645 Blaisdell, J. M.: private communication, 2019.

Cowtan, K., Hausfather, Z., Hawkins, E., Jacobs, P., Mann, M. E., Miller, S. K., Steinman, B. A., Stolpe, M. B., and Way, R. G.: Robust comparison of climate models with observations using blended land air and ocean sea surface temperatures, Geophysical Research Letters, 42, 6526–6534, https://doi.org/10.1002/2015gl064888, 2015.

Dee, D. P., Uppala, S. M., Simmons, A. J., Berrisford, P., Poli, P., Kobayashi, S., Andrae, U., Balmaseda, M. A., Balsamo, G., Bauer, P., Bech-
650 told, P., Beljaars, A. C. M., Berg, L. v. d., Bidlot, J., Bormann, N., Delsol, C., Dragani, R., Fuentes, M., Geer, A. J., Haimberger, L., Healy, S. B., Hersbach, H., Hólm, E. V., Isaksen, L., Kållberg, P., Köhler, M., Matricardi, M., McNally, A. P., Monge-Sanz, B. M., Morcrette, J., Park, B., Peubey, C., Rosnay, P. d., Tavolato, C., Thépaut, J., and Vitart, F.: The ERA-Interim reanalysis: configuration and performance of the data assimilation system, Quarterly Journal of the Royal Meteorological Society, 137, 553–597, https://doi.org/10.1002/qj.828, https://doi.org/10.1002/qj.828, 2011.

655 DeSouza-Machado, S., Strow, L., Motteler, H., and Hannon, S.: kCARTA: A fast pseudo line-by-line radiative transfer algo-rithmwith analytic Jacobians, fluxes, Non-Local ThermodynamicEquilibrium and scattering for the infrared, Atmos. Meas. Tech., https://doi.org/10.5194/amt-2019-282, accepted for publication, 2019.

ESRL: Combined Chloroflurocarbon-12 data from the NOAA/ESRL Global Monitoring Division.

Fiedler, E. K., McLaren, A., Banzon, V., Brasnett, B., Ishizaki, S., Kennedy, J., Rayner, N., Roberts-Jones, J., Corlett, G., Merchant, C. J., and
660 Donlon, C.: Intercomparison of long-term sea surface temperature analyses using the GHRSST Multi-Product Ensemble (GMPE) system, Remote Sensing of Environment, 222, 18–33, https://doi.org/10.1016/j.rse.2018.12.015, https://doi.org/10.1016/j.rse.2018.12.015, 2019.

Gordon, I. E., Rothman, L. S., Hill, C., Kochanov, R. V., Tan, Y., Bernath, P. F., Birk, M., Boudon, V., Campargue, A., Chance, K. V., Drouin, B. J., Flaud, J. M., Gamache, R. R., Hodges, J. T., Jacquemart, D., Perevalov, V. I., Perrin, A., Shine, K. P., Smith, M. A. H., Tennyson, J., Toon, G. C., Tran, H., Tyuterev, V. G., Barbe, A., Császár, A. G., Devi, V. M., Furtenbacher, T., Harrison, J. J., Hartmann, J. M., Jolly, A.,
665 Johnson, T. J., Karman, T., Kleiner, I., Kyuberis, A. A., Loos, J., Lyulin, O. M., Massie, S. T., Mikhailenko, S. N., Moazzen-Ahmadi, N., Müller, H. S. P., Naumenko, O. V., Nikitin, A. V., Polyansky, O. L., Rey, M., Rotger, M., Sharpe, S. W., Sung, K., Starikova, E., Tashkun,

S. A., Auwera, J. V., Wagner, G., Wilzewski, J., Wcisło, P., Yu, S., and Zak, E. J.: The HITRAN2016 molecular spectroscopic database, Journal of Quantitative Spectroscopy and Radiative Transfer, 203, 3–69, https://doi.org/10.1016/j.jqsrt.2017.06.038, 2017.

Hansen, J., Ruedy, R., Sato, M., and Lo, K.: GLOBAL SURFACE TEMPERATURE CHANGE, Reviews of Geophysics, 48, 670 https://doi.org/10.1029/2010RG000345, https://agupubs.onlinelibrary.wiley.com/doi/abs/10.1029/2010RG000345, 2010.

Manning, E. M., Strow, L. L., and Aumann, H. H.: AIRS version 6.6 and version 7 level-1C products, in: Earth Observing Systems XXIV, edited by Butler, J. J., Xiong, X. J., and Gu, X., vol. 11127, pp. 247 – 253, International Society for Optics and Photonics, SPIE, https://doi.org/10.1117/12.2529400, https://doi.org/10.1117/12.2529400, 2019.

Masarie, K. A. and Tans, P. P.: Extension and integration of atmospheric carbon dioxide data into a globally consistent measurement 675 record, Journal of Geophysical Research: Atmospheres, 100, 11 593–11 610, https://doi.org/10.1029/95JD00859, https://doi.org/10.1029/95JD00859, 1995.

Masson-Delmotte, V., Zhai, P., Pörtner, H. O., Roberts, D., Skea, J., Shukla, P. R., Pirani, A., Moufouma-Okia, W., Péan, C., Pidcock, R., Connors, S., Matthews, J. B. R., Chen, Y., Zhou, X., Gomis, M. I., Lonnoy, E., Maycock, T., Tignor, M., and (eds.), W.: IPCC, 2018: Summary for Policymakers. In: Global warming of 1.5°C. An IPCC Special Report on the impacts of global warming of 1.5°C above 680 pre-industrial levels and related global greenhouse gas emission pathways, in the context of strengthening the global response to the threat of climate change, sustainable development, and efforts to eradicate poverty, Tech. rep., World Meteorological Organization, 2018.

Morice, C. P., Kennedy, J. J., Rayner, N. A., and Jones, P. D.: Quantifying uncertainties in global and regional temperature change using an ensemble of observational estimates: The HadCRUT4 data set, Journal of Geophysical Research: Atmospheres, 117, https://doi.org/10.1029/2011JD017187, https://agupubs.onlinelibrary.wiley.com/doi/abs/10.1029/2011JD017187, 2012.

685 Rodgers, C. D.: Retrieval of atmospheric temperature and composition from remote measurements of thermal radiation, Reviews of Geophysics, 14, 609–624, https://doi.org/10.1029/RG014i004p00609, https://agupubs.onlinelibrary.wiley.com/doi/abs/10.1029/RG014i004p00609, 1976.

Santer, B. D., Wigley, T. M. L., Boyle, J. S., Gaffen, D. J., Hnilo, J. J., Nychka, D., Parker, D. E., and Taylor, K. E.: Statistical significance of trends and trend differences in layer-average atmospheric temperature time series, Journal of Geophysical Research: Atmospheres, 105, 690 7337–7356, https://doi.org/10.1029/1999JD901105, https://doi.org/10.1029/1999JD901105, 2000.

Stark, J. D., Donlon, C. J., Martin, M. J., and McCulloch, M. E.: Ostia: An operational, high resolution, real time, global sea surface temperature analysis system, OCEANS 2007 - Europe, pp. 1–4, https://doi.org/10.1109/OCEANSE.2007.4302251, https://doi.org/10.1109/OCEANSE.2007.4302251, 2007.

Steck, T.: Methods for determining regularization for atmospheric retrieval problems., Applied Optics, 41, 1788–97, 2002.

695 Strow, L., Motteler, H. E., Benson, R. G., Hannon, S. E., and Souza-Machado, S. D.: Fast computation of monochromatic infrared atmospheric transmittances using compressed look-up tables, Journal of Quantitative Spectroscopy and Radiative Transfer, 59, 481–493, https://doi.org/10.1016/S0022-4073(97)00169-6, https://doi.org/10.1016/S0022-4073(97)00169-6, 1998.

Strow, L. L., Hannon, S. E., Souza-Machado, S. D., Motteler, H. E., and Tobin, D.: An Overview of the AIRS Radiative Transfer Model, IEEE Transactions on Geoscience and Remote Sensing, 41, 303, https://doi.org/10.1109/TGRS.2002.808244, https://doi.org/10.1109/700 TGRS.2002.808244, 2003.

Strow, L. L., Hannon, S. E., Machado, S. D., Motteler, H. E., and Tobin, D. C.: Validation of the Atmospheric Infrared Sounder radiative transfer algorithm, Journal of Geophysical Research: Atmospheres (1984–2012), 111, https://doi.org/10.1029/2005JD006146, https://doi.org/10.1029/2005JD006146, 2006.

Susskind, J., Blaisdell, J. M., and Iredell, L.: Improved methodology for surface and atmospheric soundings, error estimates, and quality
705   control procedures: the atmospheric infrared sounder science team version-6 retrieval algorithm, Journal of Applied Remote Sensing, 8,
084 994–084 994, https://doi.org/10.1117/1.JRS.8.084994, https://doi.org/10.1117/1.JRS.8.084994, 2014.

Susskind, J., Schmidt, G. A., Lee, J. N., and Iredell, L.: Recent global warming as confirmed by AIRS, Environmental Research Letters, 14,
044 030, https://doi.org/10.1088/1748-9326/aafd4e, https://doi.org/10.1088/1748-9326/aafd4e, 2019.

Tans, P. and Keeling, R.: Trends in Atmospheric Carbon Dioxide, http://www.esrl.noaa.gov/gmd/ccgg/trends/.